Unsteady characteristics of a slat-cove flow field

Kyle A. Pascioni* and Louis N. Cattafesta
Florida Center for Advanced Aero-Propulsion, Florida State University, Tallahassee, Florida 32310, USA

(Received 16 June 2017; published 29 March 2018)

The leading-edge slat of a multielement wing is a significant contributor to the acoustic signature of an aircraft during the approach phase of the flight path. An experimental study of the two-dimensional 30P30N geometry is undertaken to further understand the flow physics and specific noise source mechanisms. The mean statistics from particle image velocimetry (PIV) shows the differences in the flow field with angle of attack, including the interaction between the cove and trailing-edge flow. Phase-locked PIV successfully links narrow-band peaks found in the surface pressure spectrum to shear layer instabilities and also reveals that a bulk cove oscillation at a Strouhal number based on a slat chord of 0.15 exists, indicative of shear layer flapping. Unsteady surface pressure measurements are documented and used to estimate spanwise coherence length scales. A narrow-band frequency prediction scheme is also tested and found to agree well with the data. Furthermore, higher-order spectral analysis suggests that nonlinear effects cause additional peaks to arise in the power spectrum, particularly at low angles of attack.

DOI: 10.1103/PhysRevFluids.3.034607

I. INTRODUCTION

Along with the landing gear, a deployed high-lift system delivers a large portion of the radiated noise from an aircraft during approach. The leading-edge slat is often the dominant noise contributor associated with the wing. While flap-side-edge noise can be a more intense source, the slat is distributed, resulting in a greater far-field effect upon integration [1].

To study slat noise, a number of approaches have been adopted. Flyover measurements are typically reserved for source ranking with results being configuration dependent. Scaled wind tunnel acoustic tests often allow for greater insight. Isolating the wing in an anechoic facility is a common approach to simulate free space while removing sources tied to other parts of the aircraft. Through the use of beamforming techniques, more accurate trends can be established from parametric studies in terms of flow speed, angle of attack, etc. For instance, slat noise is found to collapse between a Mach number power of 4 and 5 [2–5]. For the geometry used herein, the overall sound pressure levels reduce with increasing angle of attack in the range found in actual flight [5,6]. These findings can then be used to correlate not only gross aircraft characteristics with acoustic radiation but also flow quantities for slat noise prediction [7].

Several studies have also quantified noise emission sensitivity with relative element positions. Reference [8] describes the peak noise level to be 20 dB higher at a slat deflection of 25° relative to a 9° setting on a NACA 63_2-215 airfoil. With the same airfoil geometry, Ref. [2] found similar results with slat deflection while identifying an increase in levels at high frequency. The gap setting was also varied and found to modify the low-frequency behavior. Specifically, reducing the gap decreased the levels and completely closing the gap resulted in the largest reduction of approximately 14 dB.

*kyle.pascioni@nianet.org, currently at National Institute of Aerospace, 100 Exploration Way, Hampton, VA 23666, USA.

Unfortunately, closing the gap degrades aerodynamic performance too much to be considered as an effective noise reduction technique. Pagani *et al.* [9] give an extensive noise study of geometry, specifically for the 30P30N configuration. They show that not only do narrow-band peaks decrease with the angle of attack, but also that the peak amplitude decreases with increasing gap and overlap. In line with [2], Pagani *et al.* [9] also find that higher slat deflections result in an increase in high-frequency noise. To this end, Ref. [10] uses an approach for noise prediction similar to that in [7] but including slat and flap deflection settings. More recently, Ref. [11] derived a slat noise model from the theory of aerodynamic sound generation using an acoustic analogy that showed good agreement with measurements.

Although far-field measurements are crucial to maturation of noise prediction methods, relating the flow physics to far-field trends similar to those just described has the potential to produce much more accurate prediction tools. Understanding the underlying source mechanisms also benefits noise reduction concepts by directing the design in a more straightforward fashion. Time accurate numerical methods have shown an increasing level of fidelity in this regard. Both [12] and [13] showed strong evidence that slat trailing-edge shedding produces a high-Strouhal-number spectral peak ($20 < \mathrm{St}_s < 40$, where the characteristic length scale is the slat chord). In addition, strong narrow-band peaks in the mid-Strouhal-number range ($1 < \mathrm{St}_s < 5$) have been observed in both the simulated near-field surface pressure spectra and far-field spectra and have been linked to a flow-acoustic feedback of slat-cove shear layer instabilities [14]. This phenomenon is analogous to Rossiter modes [15] in open cavity flow. Unfortunately, simulations and scaled experiments (this work included) are typically performed at Reynolds numbers $O(10)$ smaller than actual flight. Given the fact that very little evidence of these narrow-band features is found in actual flight test data, a strong Reynolds-number dependence is possible. However, to conserve expense, code validation and enhancement of numerical prediction tools can be effectively pursued at lower Reynolds number (see, e.g., [16]).

Slat noise is also known to have a broadband component with a peak in the Strouhal-number range close to unity. Choudhari and Khorrami [17] attribute this to unsteady vortical structures produced by the cove shear layer interacting with the airfoil surfaces. This idea is corroborated by Knacke and Thiele [18], who used statistical correlation techniques to provide evidence that the principal source of noise is due to unsteady structures interacting with the slat trailing edge. Numerical methods have limitations, however, and must be accompanied by experiments in order to fully understand slat-cove flow. This work characterizes the unsteady slat flow field using detailed experiments that combine particle image velocimetry (PIV) with surface pressure transducers, thereby extending the results of [19].

A simplified three-element configuration will be used, namely, the 30P30N two-dimensional airfoil. Several processing techniques are performed on the acquired data and will be discussed in the following sections. The contributions of this paper are twofold: to provide (i) an improved understanding of the flow physics associated with slat-cove flow, particularly how the flow-induced noise sources themselves and their interactions change with the angle of attack, and (ii) a high-quality benchmark database to catalyze the maturation of numerical and theoretical prediction tools. The experimental setup is first described along with the mean aerodynamic conditions. Particle image velocimetry and unsteady surface pressure acquisition and processing techniques are then presented. Finally, a discussion of the results will be given, followed by conclusions.

II. EXPERIMENTAL FACILITY AND AIRFOIL

A. Experimental facility

The Florida State Aeroacoustic Tunnel is an open-circuit anechoic wind tunnel capable of freestream flow speeds from 5 to 75 m/s. The test section has dimensions of $0.914 \times 1.219 \times 3.048$ m^3, which correspond to the airfoil spanwise, normal, and flow directions, respectively. Flow nonuniformity is measured to be less than 1% and turbulence intensity high-pass filtered at 10 Hz is less than 0.1% for all flow speeds. For additional details, the reader is referred to [20].

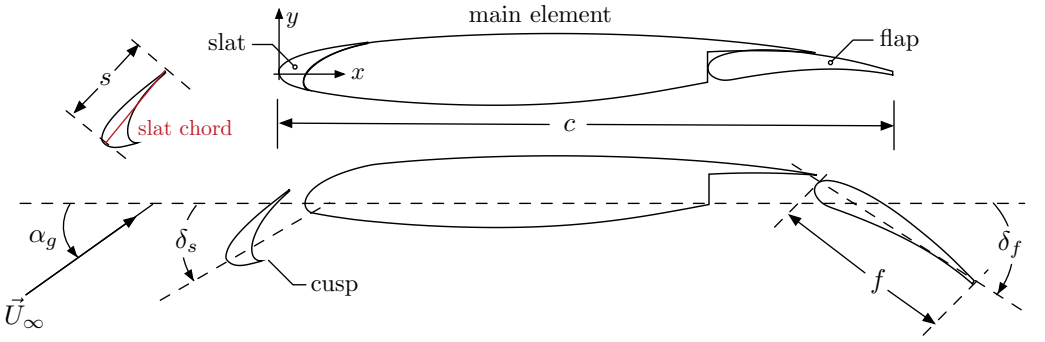

FIG. 1. Airfoil section geometry of the 30P30N high-lift configuration defining nomenclature. The gap g and overhang o settings are fixed at $g_s = 2.95\%$ and $o_s = -2.5\%$ and at $g_f = 1.27\%$ and $o_f = 0.25\%$ for the slat and flap, respectively, based on percentage of the stowed chord c. Here δ_s,$\delta_f = 30^\circ$, $s = 0.15c$, and $f = 0.3c$. The reader is referred to [21] for geometric constraints not explicitly shown in the figure. Note that the coordinate system origin is at the leading edge of the stowed airfoil.

The test section can take the form of an open-jet, closed-wall, or Kevlar wall test section. In this work the closed-wall test section is leveraged to allow optical access for laser measurement techniques. In addition, the Kevlar test section is utilized to allow acoustic array measurements of the far field. While far-field acoustic data are not the focus of the present paper, the unsteady surface pressure from this experimental configuration will be used extensively. The differences imposed by the various wall boundary conditions will be examined, allowing comparison between closed-wall, Kevlar, and free-air equivalents.

B. Airfoil geometry

The high-lift airfoil geometry is known as the MD-30P30N configuration consisting of a leading-edge slat, a main wing, and a full span trailing-edge flap. The cross section is shown in Fig. 1 along with geometric nomenclature. This geometry has been studied extensively in the literature, beginning with [21], directed to enhance numerical prediction tools of mean aerodynamic conditions. More recently, the 30P30N configuration has been chosen as a canonical multielement geometry to duly enhance aeroacoustic prediction capabilities and understand the unsteady flow characteristics [16].

The physical model is unswept (two dimensional) with a stowed chord $c = 0.457$ m and slat and flap chords $s = 0.15c$ and $f = 0.30c$, respectively. Here c is the length scale used to define the Reynolds number. Deflection angles of the leading- and trailing-edge elements are fixed at 30° (δ_s and δ_f) relative to their stowed positions. The slat trailing edge is blunt with a thickness of 0.762 mm, and the remaining geometric parameters, e.g., gap and overhang, are identical to those defined in [22]. Spanning the full extent of the test section allows an aspect ratio $b/c = 2$. Two in-flow flap brackets are located on the airfoil pressure side at $y/b = \pm 1/3$, while the slat is fixed to the main wing using out-of-flow brackets. It should be noted that the airfoil surface is in a clean configuration, i.e., without the use of boundary layer trips. The rationale of this decision is due to the fact that these data will provide insight into computational work that is performed at the same Reynolds and Mach numbers [16], making the use of a forced transition unnecessary.

C. Mean aerodynamic conditions

Due to the ambiguity in the relationship between aerodynamic conditions and angle of attack, it is helpful to provide mean aerodynamic coefficients that describe the flow field. Figure 2 shows section lift coefficients as a function of airfoil element and geometric angle of attack in the closed-wall test section α_h. Note that α_k will be used to denote the geometric angle of attack in the Kevlar test section. The values are computed using trapezoidal integration of the center-span static pressure taps. Particle

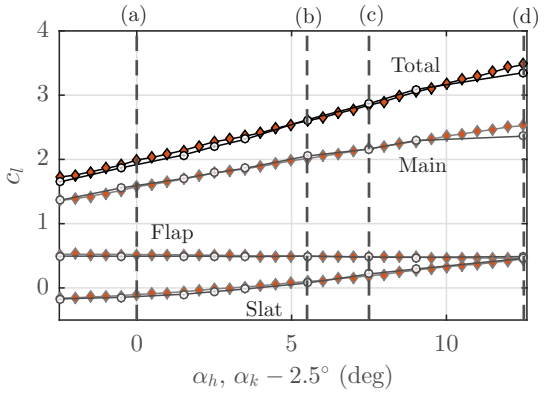

FIG. 2. Individual element and total section lift coefficient for various angles of attack. PIV is available at the highlighted angles: (a) $\alpha_h = 0^\circ$, (b) $\alpha_h = 5.5^\circ$, (c) $\alpha_h = 7.5^\circ$, and (d) $\alpha_h = 12.5^\circ$. The red markers denote results from the Kevlar test section and white markers are from the hard-wall test section. The nominal uncertainty in c_l is ± 0.03.

image velocimetry, which will be discussed shortly, is performed at the four highlighted angles of attack. Figure 3 plots the mean surface pressure distribution of these four cases. The flap loading is relatively insensitive to angle of attack, consistent with previous work [3,23,24]. The fore portion of the main element exhibits an increase in loading with angle of attack, with the sharp adverse pressure gradient limited by the counterrotating circulation of the slat.

In addition to the section lift coefficient, the Kevlar test section configuration was found to match both C_p distributions along the entire airfoil and $C'_{p,\mathrm{rms}}$ on the slat body by only modifying the geometric angle of attack. At low and moderate angles, a 2.5° increase is necessary in the Kevlar section, which increases to approximately 3° at high angles [5]. The present PIV results are measured in the hard-wall test section and are accompanied by unsteady surface pressure data from the Kevlar test section. To avoid confusion, the angle of attack will be given in terms of the hard-wall case, which is the reason for the subscript α_h.

Spanwise uniformity of the mean flow is difficult to obtain for low-aspect-ratio high-lift tests. Suction techniques have been used for aerodynamic studies [19,25] and more recently for acoustic surveys [4] to minimize flow separation on the tunnel floor and ceiling ensuring the flow field is

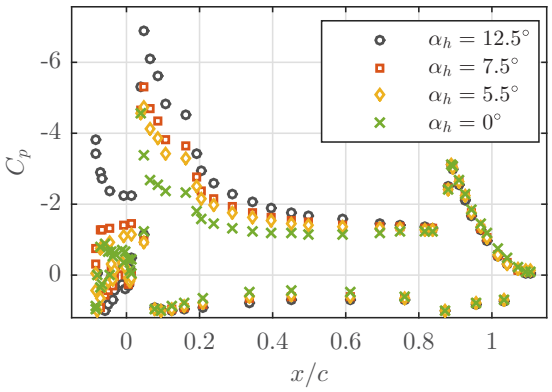

FIG. 3. Centerline mean surface pressure distribution for various angles of attack at $\mathrm{Re}_c = 1.71 \times 10^6$. The nominal uncertainty in C_p is ± 0.02.

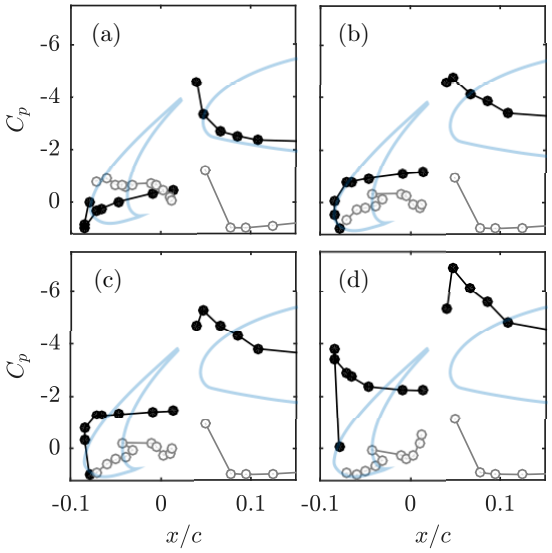

FIG. 4. Center-span mean surface pressure coefficient at $\mathrm{Re}_c = 1.71 \times 10^6$ and (a) $\alpha_h = 0°$, (b) $\alpha_h = 5.5°$, (c) $\alpha_h = 7.5°$, and (d) $\alpha_h = 12.5°$. The gray and black lines denote the lower and upper sides of the airfoil, respectively, defined by the individual element chords per Fig. 1. The nominal uncertainty in C_p is ± 0.02.

largely two dimensional. Conversely, wall suction is not used for this work. The rationale behind this decision is due to the data provided by additional arrays of taps at $1/3$ and $2/3$ spans, proving the slat pressure distribution to be very uniform with deviations less than $0.1C_p$ even at the highest angle tested [26]. All measurements herein are well within this center $1/3$ region.

To obtain a better picture of the mean slat pressure field, Fig. 4 provides a close-up of the leading-edge portion of the airfoil. The gray and black lines denote the lower and upper sides of the airfoil, respectively. Clearly, the angle of attack range encompasses various loading distributions on the slat and main element. At low angles, the upper slat surface is less heavily loaded relative to the lower surface. Here the upper and lower surfaces are defined based on the slat chord line per Fig. 1. At $\alpha_h = 2.5°$ (not shown), both the upper and lower surfaces are nearly equally loaded. The upper surface then becomes the suction side upon further increasing the angle of attack, which corresponds to the low end of typical flight angles. This trend can be explained by the position of the leading-edge stagnation point. At low angles, the stagnation point is positioned on the upper surface. Flow wraps around and is accelerated to the cusp by the leading-edge curvature. For moderate angles of attack, the stagnation point is positioned such that acceleration is approximately equal toward the cusp and slat trailing edge. Higher angles force the stagnation point to move toward the cusp; thus, greater acceleration occurs on the upper surface toward the slat trailing edge. The position of the stagnation point will be shown to be very important in terms of the strength and path of the shear layer as well as other unsteady flow phenomena.

The test matrix included angles of attack down to $-2.5°$. Although these conditions are not found in actual flight, a great deal of information regarding the unsteady flow field can be gained. As will be shown, narrow-band spectral features of the surface pressure are most prominent at lower angles of attack, thus allowing a deeper understanding of the source mechanisms. Moreover, several trends found herein could potentially be extrapolated for studies where slat deflection settings are altered (e.g., $\delta_s < 30°$). Unless otherwise noted, the presented data are acquired at a freestream Reynolds number $\mathrm{Re}_c = 1.71 \times 10^6$ based on stowed chord c, which corresponds nominally to freestream Mach number 0.17.

III. INSTRUMENTATION AND ANALYSIS METHODS

In this section flow-field measurement instrumentation is first discussed, followed by an overview of the processing methods. Information regarding acquisition of the unsteady pressure on the slat surface is then provided. Several frequency domain tools are used for data analysis and will be reviewed here.

A. Particle image velocimetry

Two component two-dimensional PIV is performed in the vicinity of the slat. To increase the field of view without loss of resolution, two 4-megapixel cameras with 180-mm lenses are positioned side by side with a small region of overlap to stitch the vector fields during postprocessing. The resulting vector resolution is 0.35 mm ($7.67 \times 10^{-4}c$). The cameras are triggered in double frame mode using LaVision DaVis software synchronized with a 200-mJ dual pulse laser (Quantel Evergreen). Due to the slat-cove geometry, a 50:50 beam splitter is used to generate two light sheets to illuminate the entire slat cove and the trailing-edge wake. The flow is seeded with diethylhexyl sebacate (DEHS) particles, approximately 1 μm in diameter, generated using a Laskin nozzle; DEHS is compatible with the flush-mounted dynamic surface pressure sensors. Each laser beam is expanded by a cylindrical lens with sheet thickness (approximately equal to 2 mm) controlled by a pair of spherical lenses. Laser reflections on the airfoil surface are minimized via orange fluorescent tape in the slat cove (0.1 mm thick) in conjunction with 532-nm bandpass optical filters.

Postprocessing the snapshots included a (1) shift correction, to remove the effect of small camera vibrations ensuring relative position between cameras are fixed; (2) sliding background subtraction, to increase the signal-to-noise ratio and minimize intensity gradients at the interface of the two light sheets; (3) geometric masking, to define the domain of interest; (4) two iteration recursive snapshot cross correlation, to compute the velocity vector fields using 48×48 pixel window size and 50% overlap; and (5) outlier rejection, a universal detection technique developed by [27]. Statistics are computed using 2000 snapshots and found to converge after approximately 700. The uncertainty $\mathcal{U}$ of the velocity, vorticity, and turbulence kinetic energy are computed by propagating the snapshot uncertainties through the calculation of each quantity. The snapshot uncertainties are found by the method of correlation statistics [28]. For the velocity magnitude, the uncertainty is computed as $\mathcal{U}(\sqrt{u^2+v^2}/U_\infty) = 0.01$–$0.05$. The low value corresponds to regions far from the cove, while the highest uncertainty is observed in regions of high shear (e.g., the cove shear layer). Similar trends are found for the turbulence kinetic energy $\mathcal{U}(\mathcal{E}_{\text{turb}}/U_\infty^2) = (4.0 \times 10^{-4})$–$(2.0 \times 10^{-3})$ and vorticity $\mathcal{U}(\omega_z c/U_\infty) = \pm(1$–$4)$.

Although the mean flow and turbulence statistics provide useful insight into the slat flow field, it is still unclear which physical flow mechanisms generate the various narrow-band peaks found in the surface pressure spectra. Phase averaging is performed to allow such information to be extracted. A low angle of attack case $\alpha_h = 0^\circ$ is chosen due to the prominence of the narrow-band peaks in the surface pressure spectrum. Hence, the chance of success for clear structure identification is maximized. To obtain the phase average, a triple decomposition [29] is performed,

$$f(\mathbf{x},t) = \bar{f}(\mathbf{x}) + \tilde{f}(\mathbf{x},t) + f'(\mathbf{x},t), \tag{1}$$

where the first term represents the time average

$$\bar{f}(\mathbf{x}) = \lim_{N\to\infty} \frac{1}{N} \sum_{n=11}^{N} f(\mathbf{x},n) \tag{2}$$

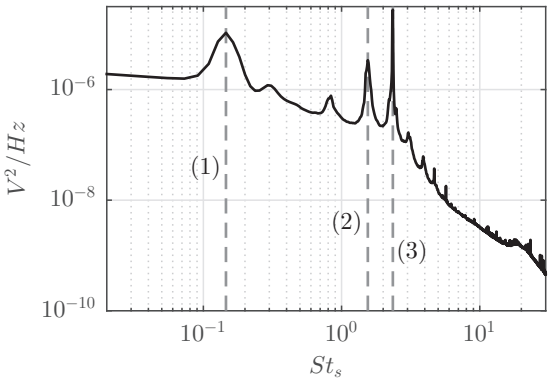

FIG. 5. Preconditioned reference signal for PIV phase averaging. Three Strouhal numbers are observed, which are labeled (1) $\mathrm{St}_s = 0.15$, (2) $\mathrm{St}_s = 1.55$, and (3) $\mathrm{St}_s = 2.36$.

of a time record using N samples. The phase average is

$$\langle f(\mathbf{x},\tau)\rangle = \lim_{N\to\infty} \frac{1}{N} \sum_{n=1}^{N} f(\mathbf{x}, t + n\tau), \tag{3}$$

where τ and N are the period and number of averages, respectively. The third term in Eq. (1) is the random turbulence fluctuation. The time average is subtracted from the phase average to extract the underlying wave component

$$\tilde{f}(\mathbf{x},\tau) = \langle f(\mathbf{x},\tau)\rangle - \bar{f}(\mathbf{x}), \tag{4}$$

which is the primary term of interest.

To gather image pairs for the phase-averaging process, the time of acquisition must be known relative to a reference signal and delayed accordingly to image the flow field at specific phases. The reference is chosen to be a signal recorded by an unsteady pressure transducer in the vicinity of the shear layer reattachment P_4 (see Fig. 7) since the frequency content of the slat-cove dynamics is thought to be sufficiently captured at this location. Figure 5 is the power spectral density of the reference showing three narrow-band peaks of interest, $\mathrm{St}_s = 0.15$, 1.55, and 2.36. Each peak represents a separate case for the triple decomposition just described. Real-time signal modification is performed to amplify each wave component of interest. The raw pressure signal is first bandpass filtered to provide a clean sinusoidal reference signal for each Strouhal number of interest. To determine the true relative phase of the image, a photodiode is simultaneously sampled with the reference to pinpoint when the PIV snapshot occurs. The photodiode signal is then superimposed on the reference as shown in Fig. 6. The zero crossings of the reference are then used to compute the time until image acquisition τ and the total period T_p. The phase is then found for the ith image pair

$$\phi_i = \frac{\tau_i}{T_{p,i}} \tag{5}$$

and subsequently converted to degrees. The uncertainty associated with ϕ does not depend on the photodiode (capable of nanosecond response) or the frame separation for a given image pair (4 μs). Rather, the analog-to-digital converter digitizing the photodiode signal is responsible for the largest uncertainty. At the specified sampling rate, the time between data points is $\Delta t = 1/65\,536$ (Hz) $= 15.3$ μs. However, compared to the shortest wave period of interest, nominally 0.5 ms, $\phi_i = \phi_{i,\mathrm{true}} \pm 5.5^\circ$, the uncertainty is deemed acceptable.

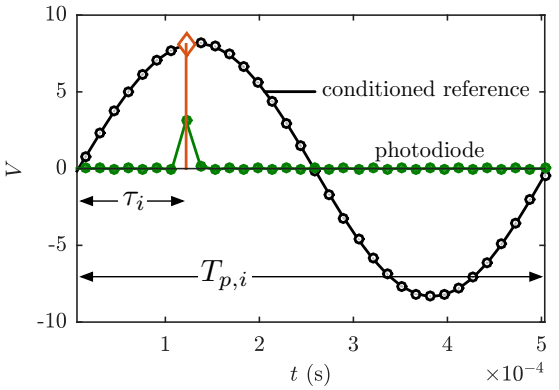

FIG. 6. Example of phase definition using the conditioned reference signal and photodiode response.

The relative phases for all image pairs in a given set are gathered and passed through a modified Thompson-Tau outlier rejection scheme [30] with a significance level of 0.05. For each phase, nominally 180 image pairs from the 200 acquired are used for averaging.

B. Unsteady surface pressure

Figure 7 and Table I define the five chordwise locations of the dynamic pressure transducers. The coordinate system is nondimensionalized by c and is equivalent to the coordinates defined in the problem statement of category 7 of the AIAA Benchmark problems for Airframe Noise Computations (BANC) workshops [16]. Spanwise information is also gathered using 11 additional transducers at location P_4. Physical spacing will be given where necessary in Sec. IV. Each Kulite pressure transducer [type LQ-062-2.5 psi (differential)] has a dedicated custom in-line amplifier and a nominal sensitivity of 3 mV/Pa. Voltage signals are digitized using National Instruments hardware (24-bit NI-4462 and NI-4498 installed in an NI-PXI-1045 chassis). All unsteady data are acquired at 204.8 kHz for 60 s. Power spectra are computed using a 12.5-Hz bin width and a 75% overlapping Hanning window resulting in 2.53% random uncertainty.

A number of spectral quantities will be used for data analysis and will be defined here. Let $X(f) = \mathcal{F}\{x(t)\}$ denote the discrete Fourier transform of the windowed pressure record $x(t)$, and similarly $Y(f) = \mathcal{F}\{y(t)\}$. The cross-spectral density of a record with length T,

$$P_{xy}(f) = \lim_{T\to\infty} \frac{1}{T} E[Y(f)X^*(f)], \tag{6}$$

where $E[\cdot]$ and an asterisk denote the expected value and the complex conjugate, respectively, is estimated between two simultaneously sampled signals. The autospectral density $P_{xx}(f)$ is the more specific case when $y(t) = x(t)$. The ordinary coherence function is also useful to describe the

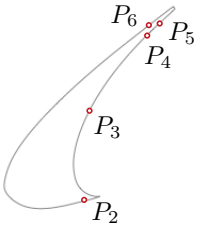

FIG. 7. Unsteady surface pressure transducer locations corresponding to Table I. Eleven additional transducers (not shown) are aligned with P_4 in a spanwise array.

TABLE I. Unsteady surface pressure transducer locations.

Location	$10^{-2}(x/c)$	$10^{-2}(y/c)$
P_2	− 3.7080	− 11.190
P_3	− 3.3573	− 5.7801
P_4	0.5816	− 0.7047
P_5	1.1533	− 0.1677
P_6	0.6712	− 0.2035

frequency-dependent relationship between two signals

$$\gamma_{xy}^2(f) = \lim_{T\to\infty} \frac{1}{T} E\left[\frac{P_{xy}(f)}{P_{xx}(f)P_{yy}(f)}\right] \tag{7}$$

such that $0 \leqslant \gamma^2 \leqslant 1$. Although these standard spectral quantities are useful, they do not provide any information about potential nonlinear effects. For this reason, higher-order spectral analysis is also introduced in an effort to describe the nonlinearities of the slat-cove flow field. Kegerise *et al.* [31] showed its importance to understand the secondary tonal features which arise due to interaction of Rossiter mode [15] pairs in an open cavity flow. The autobispectrum is defined as

$$B_{xxx}(f_i, f_j) = \lim_{T\to\infty} \frac{1}{T} E[X(f_i)X(f_j)X^*(f_i + f_j)] \tag{8}$$

to quantify quadratic coupling between frequencies f_i and f_j. The autobicoherence b_{xxx}^2 uses a normalization method similar to the ordinary coherence function using the power spectrum

$$b_{xxx}^2(f_i, f_j) = \frac{|B_{xxx}(f_i, f_j)|^2}{P_{xx}(f_i + f_j)P_{xx}(f_i)P_{xx}(f_j)}. \tag{9}$$

If two frequencies are generated by mutually independent processes, then $b^2 = 0$. If, however, two frequencies are perfectly quadratically phase coupled, $b^2 = 1$. Partial coupling can occur, $0 < b^2 < 1$, which is usually found in turbulent flows. Note that the addition of noise in a signal can reduce the true value of the bicoherence; hence, it is useful to obtain a time record long enough to allow ensemble averaging to reduce random error. In addition, the cross-bispectrum and cross-bicoherence functions quantify coupling between a pair of frequencies f_i and f_j in one signal with their algebraic sum and difference $f_i \pm f_j$ in another signal,

$$B_{yxx}(f_i, f_j) = \lim_{T\to\infty} \frac{1}{T} E[X(f_i)X(f_j)Y^*(f_i + f_j)], \tag{10}$$

$$b_{yxx}^2(f_i, f_j) = \frac{|B_{yxx}(f_i, f_j)|^2}{P_{yy}(f_i + f_j)P_{xx}(f_i)P_{xx}(f_j)}. \tag{11}$$

IV. RESULTS

A. Flow-field characteristics

A number of field quantities can be inferred from the PIV data. Figure 8 provides the time-averaged velocity magnitude contours. Although data are acquired at four angles, the two intermediate angles show very similar characteristics. Therefore, $\alpha_h = 0^\circ, 7.5^\circ$, and 12.5° will be used for this discussion. At first glance, the most notable difference with angle of attack is the shear layer path. At low angles, the higher-momentum flow upstream of the cusp pushes the shear layer farther out from the cove resulting in a larger recirculation region. Farther along, the shear layer impinges on the slat underside close to the trailing edge. The shear layer path is influenced by the accelerating mean flow around the main element. As the angle of attack is increased, the flow speed on the outside of the mixing

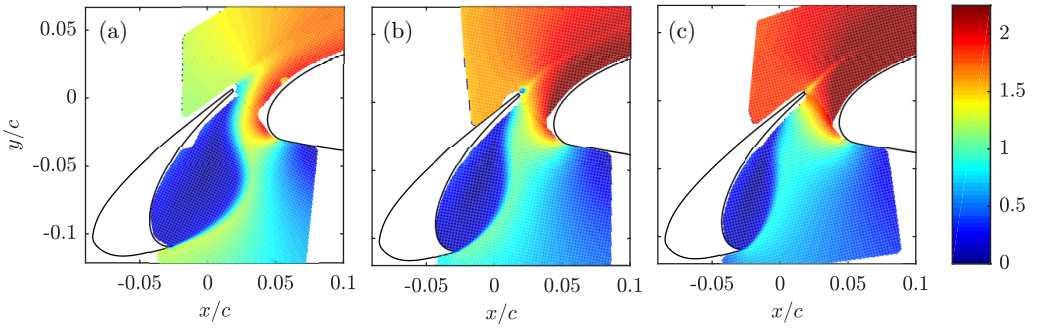

FIG. 8. Velocity magnitude $\sqrt{\langle u\rangle^2 + \langle v\rangle^2}/U_\infty$ for (a) $\alpha_h = 0°$, (b) $\alpha_h = 7.5°$, and (c) $\alpha_h = 12.5°$ at $\mathrm{Re}_c = 1.71 \times 10^6$.

layer is reduced, effectively shrinking the recirculation region and displacing the reattachment point farther from the slat trailing edge.

The slat and main element upper side also see an overall increase in flow speed imposed by the airfoil geometry with an increase in the angle of attack. Through this, unsteady characteristics can be altered, e.g., trailing-edge shedding is associated with progressively-higher-speed mean flow with an increase in angle of attack. Thus, the shedding frequency is increased when the local flow speed is higher. More details about this phenomenon will be given in Sec. IV B.

Turbulence generated by the shear layer velocity gradient is obvious in Fig. 9. Shear layer structures (which can be explicitly seen in the instantaneous vorticity plots in Fig. 13, which will be discussed later) impinge on the slat surface forming a region with large $\mathcal{E}_{\mathrm{turb}}$. At the lowest angle of attack, interaction with the trailing-edge flow creates a very large continuous $\mathcal{E}_{\mathrm{turb}}$ spot that extends beyond the trailing edge. Additionally, the contours indicate that turbulent structures are being trapped inside the cove region given the increase in $\mathcal{E}_{\mathrm{turb}}$ levels. The levels and spatial extent are found to be much larger at low angles of attack. Both qualitative and quantitative trends are in agreement with the computations performed in [24,32].

Spanwise vorticity is also computed and shown in Fig. 10. In contrast with $\mathcal{E}_{\mathrm{turb}}$, the vorticity maxima are relatively unchanged with the angle of attack. To visualize this more clearly, profiles normal to each respective shear layer (denoted by the dots in Fig. 10) are extracted. Figure 11 plots the mean vorticity at $S/S_{\mathrm{max}} = 0.1,\ 0.2, \ldots, 0.8$, where S is the arc length along the shear layer relative to its total length S_{max}. Also, the profiles are given as a function of d/c units ($-d/c$ is the cove side), corresponding to the normal distance from the shear layer center along each line. The

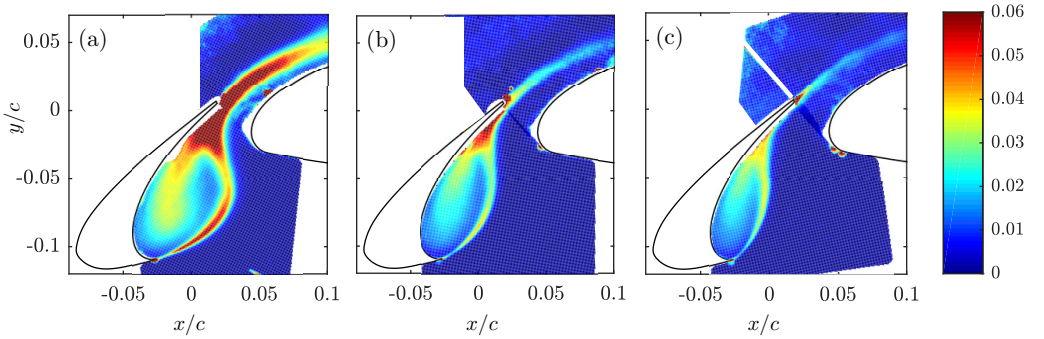

FIG. 9. Mean turbulence kinetic energy $\frac{1}{2}(\langle u'u'\rangle + \langle v'v'\rangle)/U_\infty^2$ for (a) $\alpha_h = 0°$, (b) $\alpha_h = 7.5°$, and (c) $\alpha_h = 12.5°$ at $\mathrm{Re}_c = 1.71 \times 10^6$.

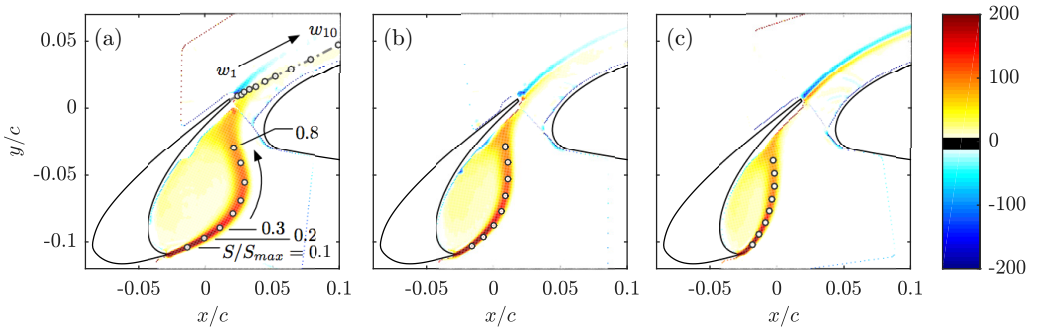

FIG. 10. Time-averaged spanwise vorticity contours $\omega_z c/U_\infty$ for (a) $\alpha_h = 0^\circ$, (b) $\alpha_h = 7.5^\circ$, and (c) $\alpha_h = 12.5^\circ$ at $\mathrm{Re}_c = 1.71 \times 10^6$.

locations of each profile center point are given in Table II. When extracting profiles relative to each shear layer, it is clear that the evolution of vorticity with $S/S_{\max}$ is nearly identical for the angles of attack studied. It should be noted that velocity magnitude and $\mathcal{E}_{\text{turb}}$ profiles extracted in a similar manner do not collapse with the angle of attack.

Figure 10 also gives additional locations for profiles to be extracted along the slat wake and are labeled $w_1, w_2, \ldots, w_{10}$. The points follow a line normal to the trailing edge emanating from its midpoint. In an effort to capture the near wake dynamics, the points are logarithmically spaced in the nondimensional coordinates as shown, which are the distances from w_1 and w_{10} to the trailing edge, respectively. Again, $-d/c$ corresponds to the upper side of the wake and $+d/c$ tends to the main element. Locations of the profile center points are given in Table III.

Along the wake, the mean vorticity best highlights the angle of attack dependence (Fig. 12). At the largest angle of attack, the mean wake profiles are consistent (but do not prove the presence of) with classic two-sided shedding initiated at the trailing edge. In other words, peak vorticity levels of opposing sign are nearly equal. On the other hand, the lowest angle of attack displays a different

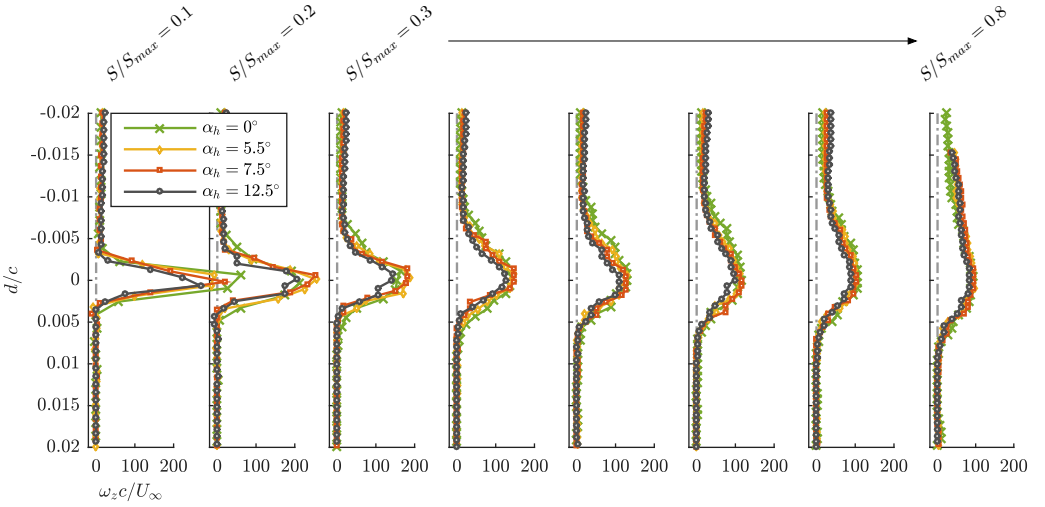

FIG. 11. Vorticity profiles of the cove shear layer, where $S/S_{\max}$ is the location of the profile center point as defined in Fig. 10 (actual coordinates of these points are given in Table II). Here d is the distance from the center of the shear layer normal to its path and $-d/c$ and $+d/c$ correspond to regions inside and outside the cove recirculation, respectively.

TABLE II. Shear layer center points of profiles.

$S/S_{\max}$	$\alpha_h = 0^\circ$ $(x/c, y/c)$	$\alpha_h = 7.5^\circ$ $(x/c, y/c)$	$\alpha_h = 12.5^\circ$ $(x/c, y/c)$
0.1	(−0.0134, − 0.1041)	(−0.0159, − 0.103)	(−0.0182, − 0.1017)
0.2	(−0.0006, − 0.0972)	(−0.0079, − 0.0963)	(−0.0129, − 0.0944)
0.3	(0.0106, − 0.0898)	(−0.0001, − 0.0874)	(−0.0083, − 0.0856)
0.4	(0.0204, − 0.0795)	(0.0062, − 0.077)	(−0.0053, − 0.0773)
0.5	(0.0264, − 0.0691)	(0.0092, − 0.0653)	(−0.0037, − 0.0682)
0.6	(0.0288, − 0.0562)	(0.0107, − 0.0529)	(−0.0021, − 0.0583)
0.7	(0.0263, − 0.0418)	(0.0107, − 0.0406)	(−0.002, − 0.049)
0.8	(0.0217, − 0.0294)	(0.0091, − 0.0284)	(−0.0027, − 0.0397)

trend. A negative peak in vorticity is present on the slat upper side, while a gradual hump is found on the lower side. This suggests that the cove shear layer structures that exit the slat–main element gap interact and disrupt wake symmetry observed at high angles. Intermediate angles corroborate this trend showing progressively weaker interaction with an increase in angle of attack. To better visualize shedding processes, Jenkins *et al.* [19] studied instantaneous vorticity snapshots, indicating the existence of three slat wake states. Two states in particular, (i) two-sided shedding and (ii) one-sided shedding with simultaneous cove structures ejecting through the slat–main element gap, occur as indicated in Fig. 13. The former situation occurs more often at the higher angle of attack, which is in agreement with the current study. Figures 13(a) and 13(b) represent the cove-wake interaction, effectively breaking up the coherent trailing-edge shedding. On the other hand, Fig. 13(c) displays clear coherent shedding uninterrupted by any structures that may have exited through the slat gap.

One other important observation should be noted, that is, the shape of the cove shear layer in Fig. 13(a). At some instances such as this one, the cove shear layer is pushed away from the trailing edge at approximately $S/S_{\max} = 0.6$, differing from the position of the mean impingement point as can be seen in Fig. 10. At several other instances, the path takes a direct route to the trailing edge. We hypothesize that the instability of the shear layer causes the downstream portion to spatially oscillate and result in a breathing, or pumping effect, of fluid through the slat gap. The following discussion, including phase averaging and the use of proper orthogonal decomposition (POD), will assist in characterizing this phenomenon.

Phase averaging the snapshots provides some very interesting results at $\alpha_h = 0^\circ$. First of all, the mechanism producing the low-frequency hump near $\mathrm{St}_s = 0.15$ in the surface pressure spectrum is identified. The four phases given in Fig. 14(a) indicate a bulk oscillation. The vertical velocity

TABLE III. Center points of slat trailing-edge wake profiles.

Location	$(x/c,\ y/c)$
w_1	(0.0247,0.0089)
w_2	(0.0267,0.01)
w_3	(0.0294,0.0114)
w_4	(0.033,0.0132)
w_5	(0.0378,0.0157)
w_6	(0.0441,0.019)
w_7	(0.0525,0.0234)
w_8	(0.0637,0.0293)
w_9	(0.0786,0.037)
w_{10}	(0.0985,0.0474)

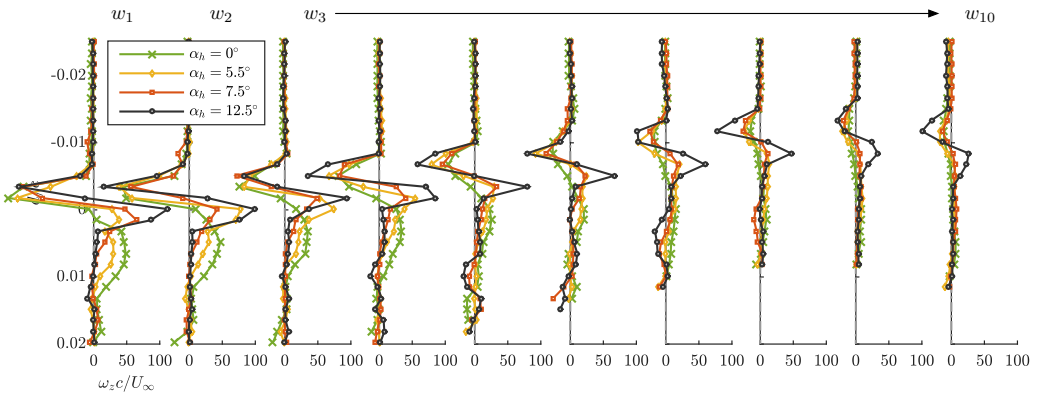

FIG. 12. Vorticity profiles of the wake shear layer following the points w_1–w_{10} as defined in Fig. 10 (actual coordinates of these points are given in Table III). Here d is the distance from the w points parallel to the slat trailing edge and $-d/c$ and $+d/c$ correspond to regions above and below these points, respectively.

of the majority of the flow in the cove is positive at $\phi = 0°$, but switches to a negative velocity at $\phi = 180°$. Furthermore, phase-locked vorticity (not shown) displays very low levels relative to the other two Strouhal numbers, suggesting that the cove flow moves in unison. The mechanism causing this oscillation can be linked to the unsteady impingement location, i.e., shear layer flapping, which will be discussed shortly using Fig. 15. The vortical shear layer structures either exit through the slat–main element gap ($\phi = 0°$) or get trapped in the cove ($\phi = 180°$). This process repeats itself in a stationary manner, with a fundamental Strouhal number of $\mathrm{St}_s = 0.15$ (nominal, as this value can change with the angle of attack).

The two remaining Strouhal numbers that are phase averaged clearly show coherent structures in the shear layer. The prediction model for cove resonance frequencies that will be discussed in Sec. IV D is consistent with these results. At $\mathrm{St}_s = 1.55$ found in Fig. 14(b), the u-velocity component switches sign two or three times along the shear layer path, while at $\mathrm{St}_s = 2.36$ in Fig. 14(c), the sign switches three or four times. This indicates that the narrow-band peak frequencies in the pressure spectra are dependent on the spatial frequency of the vortices present in the shear layer.

Note that for these phase averages, the shear layer structures are unusually large due to the coupling with the cove oscillation. The visualized structures are spread (most prominently in the direction normal to the shear layer path) relative to their true size due to the shear layer flapping. This flapping motion will now be discussed.

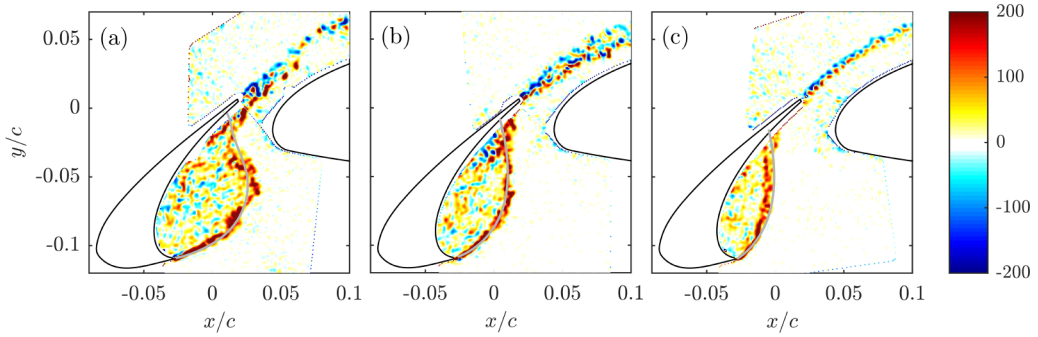

FIG. 13. Instantaneous spanwise vorticity contours $\omega_z c/U_\infty$ for (a) $\alpha_h = 0°$, (b) $\alpha_h = 7.5°$, and (c) $\alpha_h = 12.5°$ at $\mathrm{Re}_c = 1.71 \times 10^6$. The mean dividing streamline is superposed for each angle of attack.

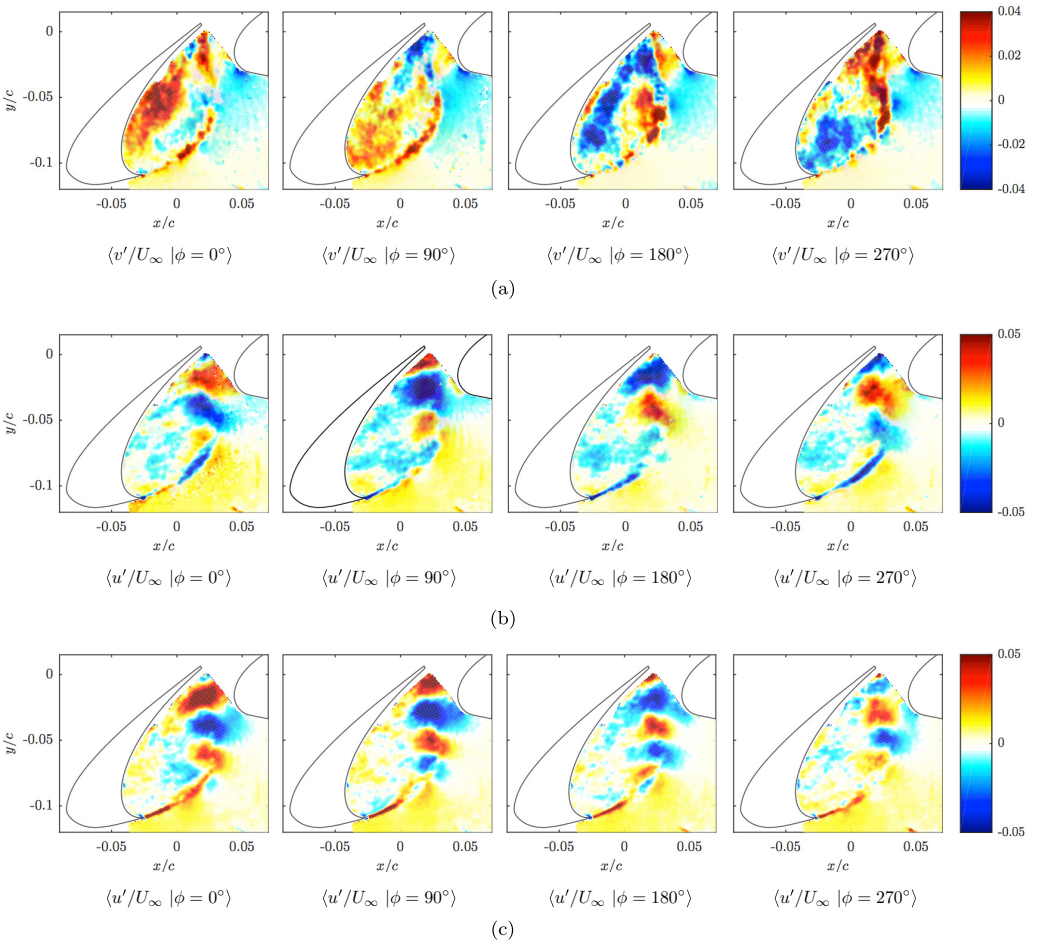

FIG. 14. Phase averaging at $\alpha_h = 0^\circ$, $\mathrm{Re}_c = 1.71 \times 10^6$, and Strouhal numbers (a) $\mathrm{St}_s = 0.15$, (b) $\mathrm{St}_s = 1.55$, and (c) $\mathrm{St}_s = 2.36$.

The spatial oscillation of the reattachment point, or breathing motion, has been documented in several other type of flows. One useful example is by Mohammad-Taifour and Weiss [33], who showed a large contraction and expansion of a turbulent separation bubble through the use of a low-dimensional representation of the flow field. Due to the similarities of a turbulent separation bubble and the present slat-cove problem, their method is repeated here.

Proper orthogonal decomposition enables the velocity field to be separated into a set of spatial modes $\boldsymbol{\varphi}(\mathbf{x})$ and temporal coefficients $a(t)$,

$$\mathbf{U}(\mathbf{x},t) = \bar{\mathbf{U}}(\mathbf{x},t) + \sum_{i=1}^{N} a_i(t)\boldsymbol{\varphi}_i(\mathbf{x}). \tag{12}$$

An approximation to this equation can be made to retain only the most energetic modes

$$\mathbf{U}(\mathbf{x},t) \approx \tilde{\mathbf{U}}(\mathbf{x},t) = \bar{\mathbf{U}}(\mathbf{x},t) + \sum_{i=1}^{r<N} a_i(t)\boldsymbol{\varphi}_i(\mathbf{x}), \tag{13}$$

where r is the chosen number of modes, an overbar denotes the mean field, and a tilde denotes a low-dimensional approximation. The method of snapshots [34] is used on the two-component

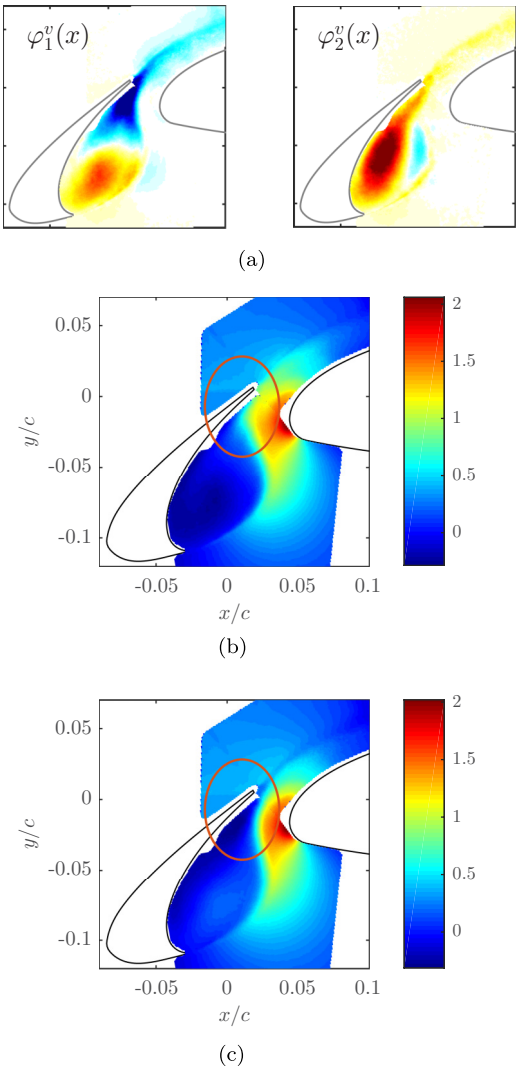

FIG. 15. The POD analysis pertaining to shear layer flapping, showing (a) the first and second v-component velocity POD mode and $\tilde{v}$ [Eq. (14)] when the temporal coefficient of the first POD mode is (b) minimum ($\tilde{v}/U_\infty|_{\min\{a_1(t)\}}$) and (c) maximum ($\tilde{v}/U_\infty|_{\max\{a_1(t)\}}$).

mean-subtracted field. The scalar components of $\boldsymbol{\varphi}(\mathbf{x})$ can be separated, which correspond to the u- and v-velocity components, denoting the nth modes as $\varphi_n^u(\mathbf{x})$ and $\varphi_n^v(\mathbf{x})$.

Upon qualitatively surveying the spatial modes, modes 1 and 2 correspond to phenomena that span the full extent of the cove and contain 10.3% and 7.7% of the total energy using 2000 snapshots, respectively, at $\alpha_h = 0^\circ$. Figure 15(a) illustrates this best by plotting the v component of the first two modes. Almost all of the remaining modes are found to highlight the shear layer itself or the slat wake as opposed to the recirculation region. The resemblance of Fig. 15(a) with the structures found by phase averaging at $\mathrm{St}_s = 0.15$ indicates that the first two spatial modes at least partially capture the cove oscillation. Therefore, following [33], we reconstruct the flow using just the first mode. Figures 15(b) and 15(c) display the v component of velocity, i.e.,

$$\tilde{v}(\mathbf{x},t) = \bar{v}(\mathbf{x},t) + a_1(t)\varphi_1^v(\mathbf{x}), \tag{14}$$

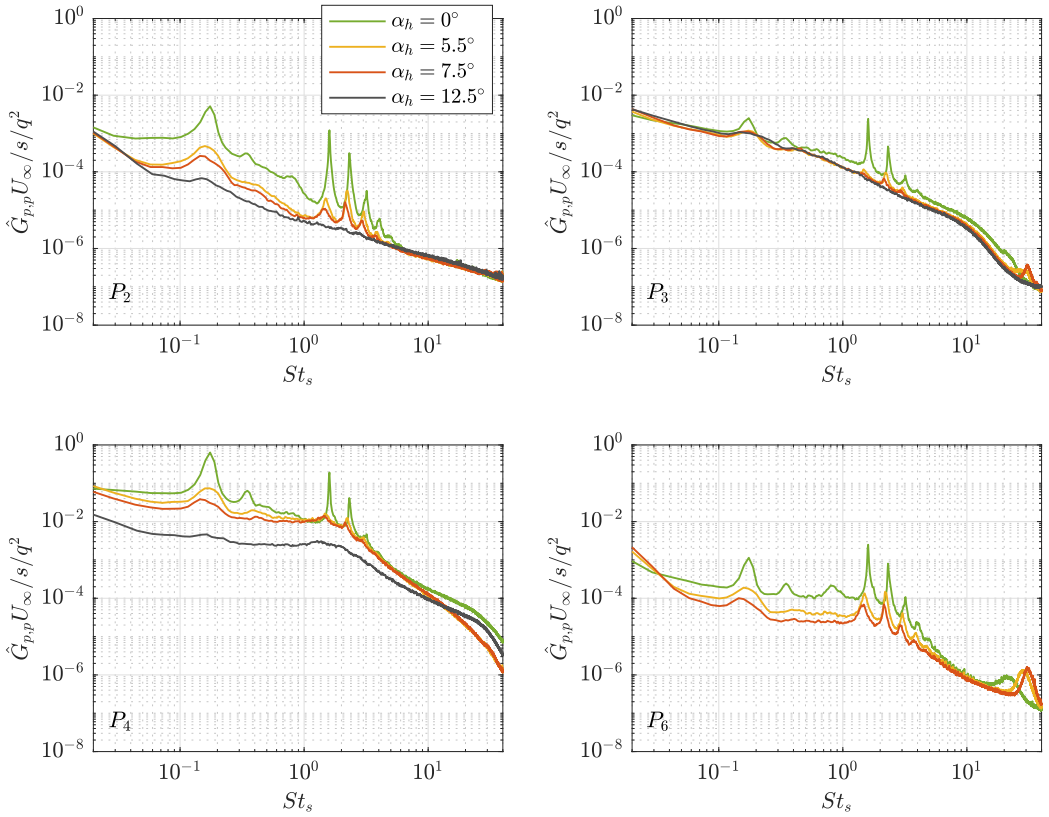

FIG. 16. Variation of unsteady surface pressure spectra with angle of attack at locations P_2–P_4 and P_6 for $\mathrm{Re}_c = 1.71 \times 10^6$ nondimensionalized by dynamic pressure q, slat chord s, and freestream velocity U_∞.

at specific instances, namely, when the temporal coefficient a_1 reaches its minimum and maximum values. The reason is to establish bounds of how the bulk cove oscillation affects the flow. Only the first mode is chosen due to the fact that the $\min\{a_1(t)\}$ and $\min\{a_2(t)\}$ occur at different instances. Satisfying the minimum requirement shows a clear indication that the reattachment point is displaced away from the trailing edge, far from its mean location. On the other hand, the maximum condition shows the shear layer to assume a path on the opposite side of its mean location. Furthermore, the cove exhibits a lower aspect ratio when $a_1(t)$ is smallest, while the cove is thinner when $a_1(t)$ is at its maximum, similar to the mean fields of higher angles of attack. Although not as prominent as the breathing motion found in [33] (where the first mode represented 30% of the total energy), it is obvious that the reattachment point is oscillating along the slat surface.

B. Unsteady surface pressure trends

Unsteady pressure signals are acquired at various chordwise locations and summarized in Fig. 16. The broadband levels vary by an order of magnitude when comparing locations inside and outside the slat cove. The largest overall levels are near the shear layer reattachment point, suggesting that the cove reattachment region is the source of the most prominent fluctuations. The suction side exhibits the lowest levels of pressure fluctuations as they are not directly exposed to the high-amplitude vorticity structures in the slat shear layer. Narrow-band peaks are present in the frequency spectra at all locations with increasing prominence at smaller angles of attack. The peaks in the Strouhal-number range of 1–3 are related to shear layer instabilities as evidenced in Sec. IV A. The spectral peaks in

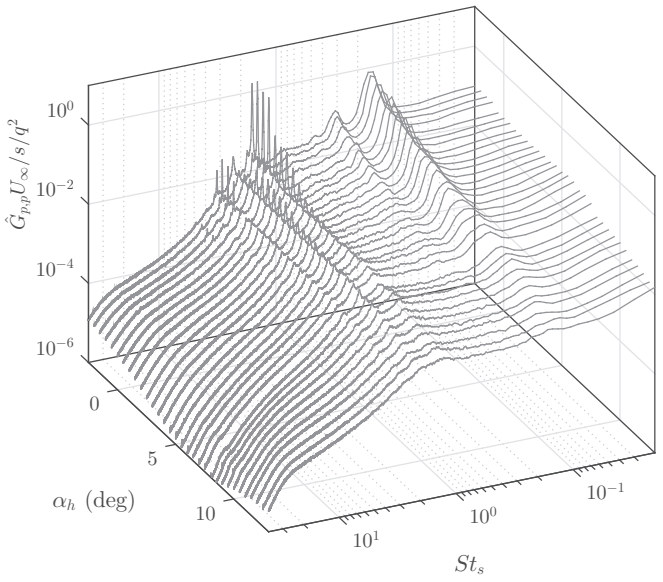

FIG. 17. Variation of narrow-band peak amplitude with angle of attack at location P_4 for $\mathrm{Re}_c = 1.71 \times 10^6$, nondimensionalized by dynamic pressure q, slat chord s, and freestream velocity U_∞.

P_2 and P_6 (outside the cove as shown in Fig. 7) suggest that part of the pressure signals consist of acoustic waves that extend beyond the cove as opposed to hydrodynamic fluctuations. Hence, these two sensors can be thought of as near-field microphones.

As noted, the amplitudes of the narrow-band peaks decrease with angle of attack, which is consistent with far-field acoustic measurements [5,6]. Upon studying the mean flow field, these levels are consistent with the shear layer properties, most notably the much higher $\mathcal{E}_{\mathrm{turb}}$ at low angles. Other influences, such as the flow-acoustic resonance system [35] and acoustic resonance properties of the airfoil geometry itself [36], are also expected to have an impact on the peak levels.

The broadband signature is likely a by-product of shear layer structures impinging and subsequently distorting as they exit through the slat gap. Additionally, acoustic scattering off the trailing edge can also have an impact on the broadband component. Such a hypothesis is in agreement with the flow phenomena indicated by the PIV data. In any case, the broadband levels at P_2 and P_6 are found to collapse with the angle of attack for $\mathrm{St}_s > 6$. Therefore, $\mathrm{St}_s > 6$ are likely associated with a mechanism that is relatively insensitive to the angle of attack.

Trailing-edge shedding has been found to have a high Strouhal number ($20 < \mathrm{St}_s < 40$). The signal measured by P_6 in Fig. 16 displays this hump and varies in Strouhal number with the angle of attack. Although not shown, the hump collapses exceptionally well at a Strouhal number of 0.2 when it is redefined using the trailing-edge thickness and the local flow velocity extracted from the PIV data. As mentioned earlier, the wake is associated with a progressively higher mean velocity field which is the result of acceleration about the main element and upper slat surface. Hence, the change in the characteristic velocity with the angle of attack used to redefine Strouhal number is justified.

Figure 17 shows the gradual change in the pressure spectrum near the reattachment location (sensor P_4) with the angle of attack. While the surface pressure spectrum is found to collapse well with flow speed and freestream dynamic pressure [22], the level of unsteadiness is found to be very sensitive to the angle of attack. For example, a 27-dB difference is found at this location between the lowest and highest angles of attack tested in these experiments (Reynolds number held constant). This angle of attack trend is consistent with far-field acoustic measurements in [3,4]. Also, the bulk

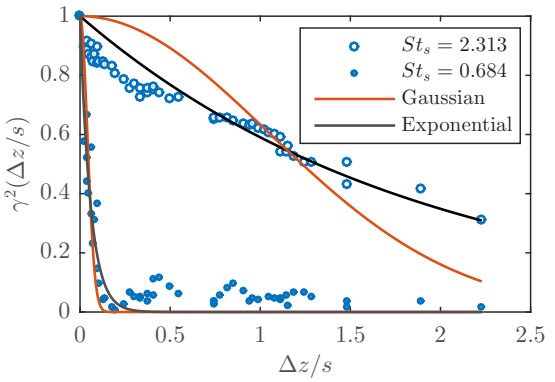

FIG. 18. Example of functional fits from Eqs. (15) and (16) for two Strouhal bins using a Gaussian and an exponential model for the $\alpha_h = 0^\circ$ case.

cove oscillation as found by the phase-locked PIV results contributes to the pressure spectrum at almost all angles of attack, but gradually decays to broadband levels at high angles.

C. Spanwise coherence length scale estimation

The intensity of noise radiation is sensitive to the spatial coherence scale of the source fluctuations at any given frequency. Therefore, the spanwise coherence characteristics of the slat pressure fluctuations are investigated in addition to their frequency spectra at individual locations. The spanwise array of transducers corresponds to the nominal chordwise position of the shear layer reattachment point P_4 (see Fig. 7). Note that these transducers are distributed across 2.22 slat chords (or 1/6 of the total airfoil span). The discussion in Sec. II C describes the spanwise uniformity of the mean flow as being found across twice this central region; thus, the following results are expected to be minimally affected by such experimental artifacts.

The coherence function per Eq. (7) is computed for all transducer pairs, i.e., $\gamma^2_{m,m'}$, where $m,m' = 1,2,\ldots,M$, $M = 11$. Note that a successful test for spanwise homogeneity of the coherence function preceded this analysis. After this calculation, the coherence as a function of Strouhal number is fit with a Gaussian model as a function of spanwise separation Δz,

$$\gamma^2(\mathrm{St}_s) = \exp\left[-\left(\frac{\Delta z}{L_{\gamma_1}(\mathrm{St}_s)}\right)^2\right], \tag{15}$$

allowing the coherence length scale L_{γ_1} to be found. Note that this fit is necessary as the coherence does not fully decay before the maximum sensor spacing is reached. Hence, integration under the coherence curve cannot be performed for several Strouhal bins (most notably the narrow-band peaks). However, the method compares well with integration techniques for broadband Strouhal numbers. Two Strouhal bins are plotted along with this function as an example in Fig. 18. For Strouhal numbers associated with the broadband component, the Gaussian function captures the trend reasonably well. However, at low angles of attack, the fit is not consistent with the data at the narrow-band peaks where the length scale can exceed that of the slat chord. Therefore, an exponential fit of the form

$$\gamma^2(\mathrm{St}_s) = \exp\left(-\frac{\Delta z}{L_{\gamma_2}(\mathrm{St}_s)}\right) \tag{16}$$

is also attempted. This length scale is denoted by L_{γ_2}. The spanwise coherence trend is more accurately captured for all frequencies with this exponential model.

Using this approach, the coherence length can be approximated for all Strouhal numbers. The results are given in Fig. 19. Differences associated with the two models L_{γ_1} and L_{γ_2} are found to

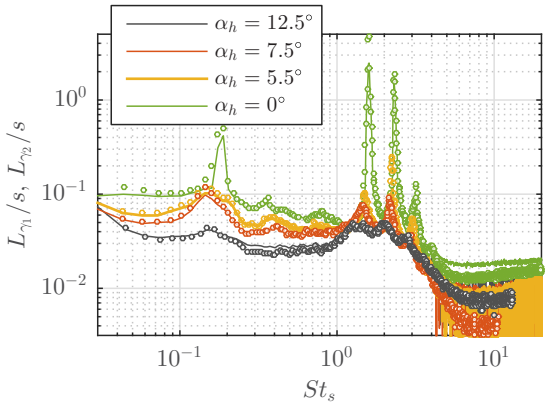

FIG. 19. Estimated spanwise coherence lengths L_{γ_1} and L_{γ_2} for four angles of attack at $\mathrm{Re}_c = 1.71 \times 10^6$, using Eqs. (15) (solid lines) and (16) (circle markers), respectively.

be small. The largest deviation of the broadband is found to be 16%. It is clear that the Strouhal numbers of the narrow-band peaks show much larger coherence length scales relative to the broadband component. More interestingly, a larger coherence length is observed at the lower angles of attack, regardless of whether the Strouhal parameter corresponds to the broadband portion of the power spectrum or to the narrow-band peaks. Care must be taken in interpreting these results due to the fact that the shear layer impingement point moves farther from the spanwise array with the angle of attack.

D. Narrow-band frequency prediction

In an effort to understand the source mechanisms of the narrow-band peaks, Terracol *et al.* [35] modified Rossiter's equation [15] for cavity tones to predict slat-cove peak frequencies. This prediction scheme has not previously been performed on the 30P30N geometry. Therefore, it will be very useful to attempt here not only to establish robustness of the method, but to provide deeper insight and validation for future analyses.

The nth narrow-band peak Strouhal number can be predicted by

$$(\mathrm{St}_s)_n = n\frac{s}{L_a}\left(\frac{1}{M + \frac{\eta_l}{\kappa_v}}\right). \tag{17}$$

Here L_a is the acoustic path length from the origin of the shear layer (slat cusp) to the impingement point, M is the freestream Mach number, $\eta_l = L_v/L_a$ is the ratio between shear layer path lengths L_v and L_a, and $\kappa_v = U_c/U_\infty$ is the nondimensional convection velocity of the shear layer. Note that Eq. (17) is the simplified version, accomplished by the fact that the mean flow velocity along L_a is negligible as it is inside the cove recirculation. The ratio of path lengths, included here, must be accounted for in slat-cove flow because L_v and L_a can differ by 20% or more, especially at low angles of attack. In other words, the predicted frequencies are very sensitive to the total loop length of the feedback system $L_v + L_a$.

To employ this prediction method, three flow-field parameters need to be determined, L_a, L_v, and U_c. For L_a, the impingement point is first approximated by following the reattachment streamline of mean flow PIV data. The presence of laser reflections in the PIV data saturates the image close to the slat element resulting in a loss of data near the surface. This gives some uncertainty in estimating the precise reattachment location. However, studying adjacent streamlines, the impingement point is estimated to within $\pm 0.016c$. The parameter L_a is found by measuring the distance from the cusp to the estimated impingement location. The convection velocity along the shear layer is typically found

TABLE IV. Measured flow parameters.

α_h	L_a/c	$\kappa_v = U_c/U_\infty$	$\eta_l = L_v/L_a$
0°	0.115	0.781	1.196
5.5°	0.1103	0.710	1.102
7.5°	0.1043	0.653	1.097
12.5°	0.089	0.543	1.060

with a two-point space-time cross correlation or the use of vortex tracking methods such as the Q criterion or Γ_2. However, time-resolved flow-field data are not available in the current study. Several methods are compared by Mohammad-Taifour and Weiss [33] to estimate the convection velocity of a large turbulent separation bubble. They find good agreement between space-time cross correlations and the time-average velocity magnitude along the path mapped by the maximum spanwise vorticity. Using this criterion and averaging along the shear layer, convection velocities are similar to those found in the simulations of [35], albeit using a different airfoil geometry. Finally, L_v is found by determining the distance traveled by the arc length of the shear layer path. Table IV summarizes these parameters for the four angles of attack where flow-field information is available.

As mentioned, PIV data are limited to four angles of attack. However, unsteady surface pressure is acquired for 32 angles of attack. Obviously, it is desirable to compare the prediction scheme for all angles where narrow-band peaks are present. Therefore, the parameters summarized in Table IV are interpolated using quadratic fits where flow-field data are not available, allowing Eq. (17) to be computed for all cases. Figure 20 shows that the prediction scheme agrees reasonably well for modes $n = 2$–6. Note that the Strouhal numbers of the first mode cannot be extracted as they are masked by broadband levels. These results show good agreement across the full experimental test matrix, with a maximum root-mean-square error between the measured and predicted Strouhal numbers of 5% occurring at mode 2. Below $\alpha_h = 6°$, this residual variance drops to less than 2.5% for all modes. Because the prediction scheme is based on the fact that feedback resonance is behind the generation of the content at these frequencies, this is strong evidence concerning the underlying physical mechanism. The level of amplification provided by the flow-acoustic feedback versus acoustic resonance of the geometry (Ref. [36] showed that longitudinal resonance can exist at frequencies that scale with the cove length) is still not clear.

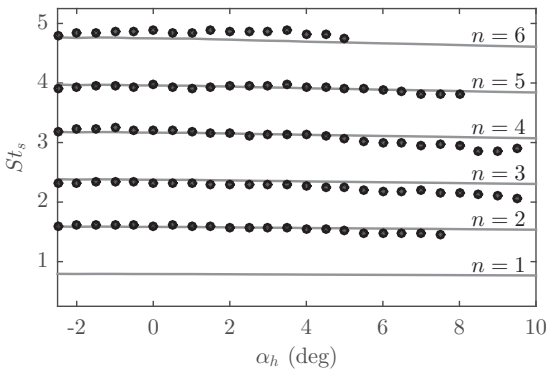

FIG. 20. Narrow-band frequency prediction comparison with measurements as a function of angle of attack.

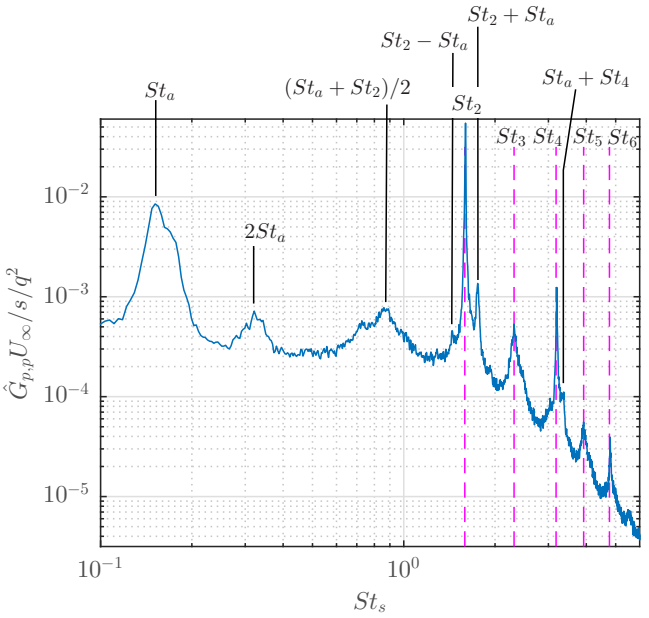

FIG. 21. Power spectral density of sensor P_6 for $\alpha_h = -2.5^\circ$ and $\mathrm{Re}_c = 1.71 \times 10^6$. The primary peaks which are approximately determined by Sec. IV D are labeled by the dashed magenta lines.

E. Higher-order spectral analysis

Higher-order spectral analysis is also introduced in an effort to quantify quadratic nonlinearities, if any, associated with the slat-cove flow field. As found in the preceding section, several narrow-band peaks in the surface pressure spectra are the result of Rossiter-like shear layer instabilities, resonating due to a flow-acoustic feedback. Also found in the spectra are auxiliary narrow-band peaks, being most prominent at low angles of attack. An example spectrum can be found in Fig. 21 from sensor P_6 at $\alpha_h = -2.5^\circ$ and $\mathrm{Re}_c = 1.71 \times 10^6$. This sensor is chosen to emphasize acoustics as it is located on the upper slat surface outside the cove (refer to Fig. 7). The lowest angle of attack with unsteady pressure data available is used to highlight potential quadratic interactions because they are most prominent. Here the bin width is set to 3.125 Hz for additional resolution and the peak Strouhal numbers that are approximately determined using the model described in Sec. IV D are labeled with dotted lines, from St_2 to St_6. These Strouhal numbers will be referred to as primary peaks for this discussion.

The autobicoherence of the same signal is plotted in Fig. 22 with several Strouhal pairs labeled. Referencing this plot, self-interaction occurs at the primary peaks (St_2,St_2), (St_3,St_3), and (St_4,St_4), indicating that these Strouhal numbers generate harmonics. From the first pair, $\mathrm{St}_2 + \mathrm{St}_2 = \mathrm{St}_4$; thus, the autospectral peak at St_4 is at least partially the result of quadratic interaction. Based on the power spectrum alone, it is unclear if this harmonic Strouhal number is generated purely as a by-product of St_2 or if coherent flow structures with a fundamental frequency of St_4 in the shear layer are responsible. For the second pair, no prominent peak in the power spectrum is found at $\mathrm{St}_3 + \mathrm{St}_3$, implying its contribution is not strong enough to overcome the broadband component of the signal. A similar situation is noted for the third Strouhal-number pair. The low-frequency cove oscillation (as evidenced by phase-locked PIV in Sec. IV A) at St_a also produces a harmonic at $2\,\mathrm{St}_a$. Given this, a peak in the autobicoherence at (St_a,St_a) is expected to be present; however, poor resolution and the large width of this peak (perhaps better characterized as a spectral hump rather than peak) inhibit this feature from being clearly revealed.

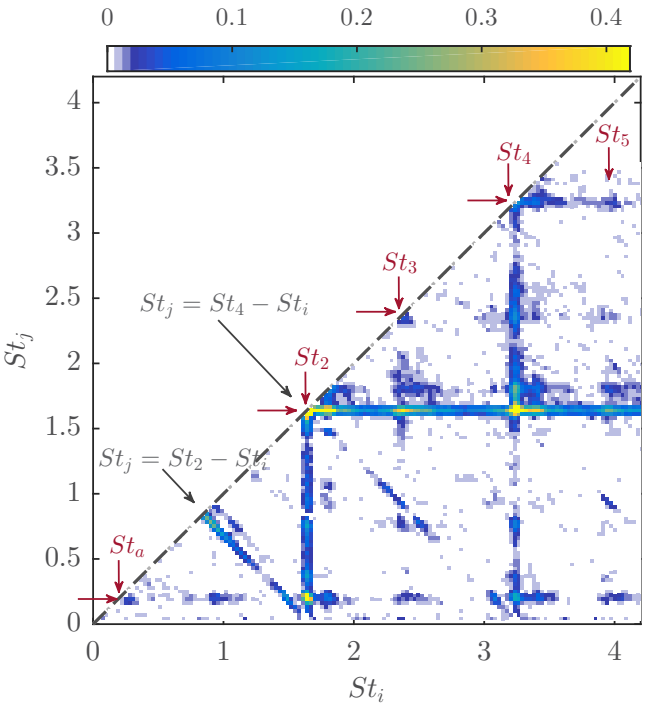

FIG. 22. Autobicoherence spectrum for the signal shown in Fig. 21. Note that the upper bound of the colormap is saturated to expose secondary features. In reality, $\max(b^2) = 0.95$ at (St_2,St_2).

The nonlinear connection between St_2 and St_4 is further supported by the change in relative strength in the power spectrum with the angle of attack. Low angles show these two peaks to be very dominant. As the angle of attack is increased, the levels of these autospectral peaks both decrease together, so much so that St_3 becomes dominant in the power spectrum.

While Eq. (17) predicts a harmonic relationship (assuming a frequency-independent convection velocity), this is not strictly borne out by the experimental data. Referencing Fig. 21, experimental Strouhal numbers are indeed described by the relationships $St_4 = 2\,St_2$ and $St_6 = 3\,St_2$, following the prediction very accurately. Conversely, St_3 and St_5 deviate slightly from this harmonic sequence. This observation will be taken advantage of in the following discussion. Note that this difference between the prediction and the Strouhal number experimentally observed is an order of magnitude larger than the spectral resolution.

In addition to self-interaction, interaction among the primary peaks occurs. The large amplitude of St_2 influences other modes displaying an autobicoherence greater than 0.25 at (St_3,St_2), (St_4,St_2), and (St_5,St_2). For the first pair, $St_3 + St_2 = St_5$. Hence, St_5 is at least partially due to this nonlinear interaction. Similarly, $St_4 + St_2 = St_6$. This is again evidence that the power spectrum level at St_6 is also partially generated by nonlinearities. If the experimental Strouhal peaks were a true harmonic sequence, it would be difficult to differentiate between pairs that result in, for example, St_5 versus St_6. Also note that the autobicoherence cannot reveal second-harmonic information. In other words, we can merely speculate that the second harmonic of St_2 (that is, $3\,St_2 = St_6$) plays a role at St_6. For the other pairs mentioned, the broadband component masks their nonlinear contributions. Given the fact that the broadband component rolls off rapidly with frequency, pairing at high frequencies is more readily observed in the power spectrum. Moreover, the dominance of St_2 and St_4 is highlighted by the fact that nonlinear interactions with these phenomena are observed over a large-Strouhal-number range (indicated by the horizontal and vertical lines in the autobicoherence).

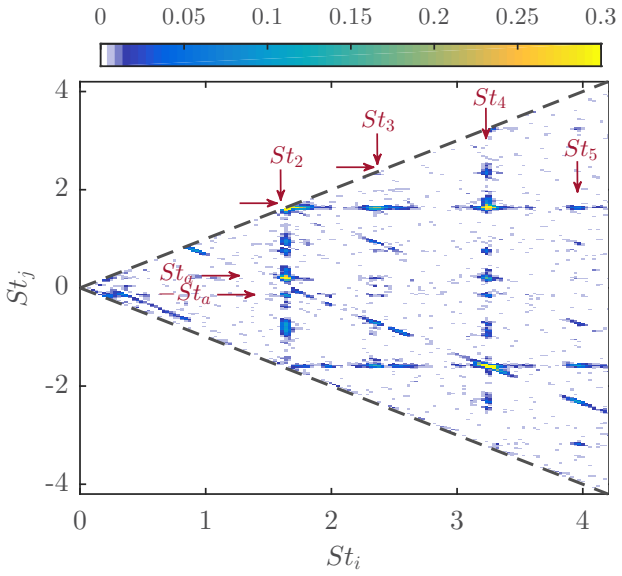

FIG. 23. Cross-bicoherence spectrum between P_2 and P_6 as shown in Fig. 7. Note that the upper bound of the colormap is saturated to expose secondary features.

Most interestingly, the primary shear layer peaks are found to be strongly coupled with the low-frequency cove oscillation St_a, contributing to the autobicoherence spectrum at $(\mathrm{St}_2,\mathrm{St}_a)$, $(\mathrm{St}_3,\mathrm{St}_a)$, $(\mathrm{St}_4,\mathrm{St}_a)$, and $(\mathrm{St}_5,\mathrm{St}_a)$. Features in the power spectrum with sum and differences of these Strouhal-number pairs are present at $\mathrm{St}_2 \pm \mathrm{St}_a$ and less obviously at $\mathrm{St}_4 \pm \mathrm{St}_a$.

The autobicoherence spectrum peak values are sensitive to the angle of attack as indicated in Figs. 24 and 25. This suggests that not only are the peak levels at the primary Strouhal numbers lower with increasing angle of attack, so too are their quadratic coupling. Visually, there are no noticeable bicoherence peaks above the noise floor beyond $\alpha_h > 6^\circ$.

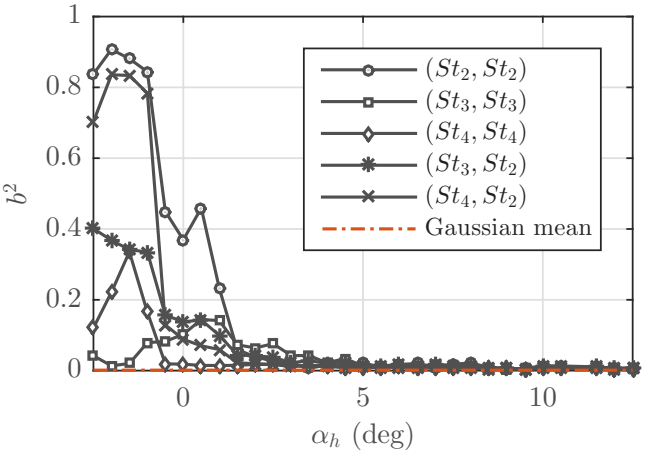

FIG. 24. Effect of angle of attack on the main autobicoherence peak Strouhal pairs involving self-interaction and resonance mode-mode interaction, using the signal acquired at P_6 and $\mathrm{Re}_c = 1.71 \times 10^6$.

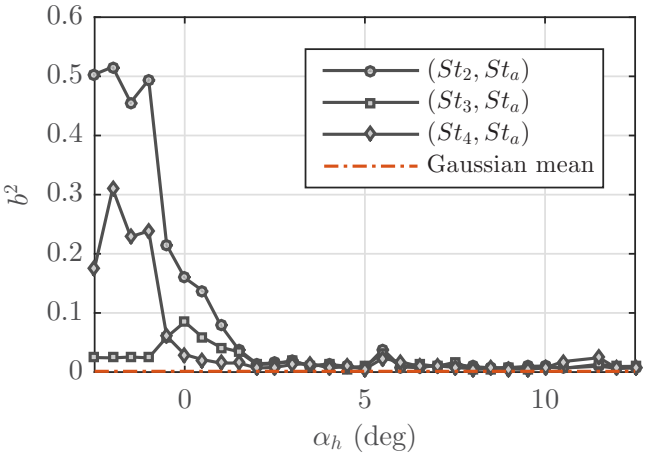

FIG. 25. Effect of angle of attack on the main autobicoherence peak Strouhal pairs involving interaction between resonance modes and the bulk cove oscillation, using the signal acquired at P_6 and $\mathrm{Re}_c = 1.71 \times 10^6$.

The cross bicoherence determines the quadratic coupling between a pair of Strouhal numbers St_i and St_j in one signal with their algebraic sum and difference $\mathrm{St}_i \pm \mathrm{St}_j$ in another signal [31]. Along with the autobicoherence, additional information can be extracted that is otherwise masked by the broadband in the power spectrum. An example between sensors P_2 and P_6 is given in Fig. 23. The unique cross-bicoherence domain is (0,0), ($\mathrm{St_{Nyq}}$, $-\mathrm{St_{Nyq}}$), and ($\mathrm{St_{Nyq}}$,$\mathrm{St_{Nyq}}$), where $\mathrm{St_{Nyq}}$ represents the Nyquist Strouhal number. Therefore, St_j can be negative, distinguishing between quadratic coupling of sum and difference pairs.

Many of the same Strouhal pairs in the autobicoherence are in the cross bicoherence. Interactions at frequencies (St_2,St_2) and (St_3,St_3) have an almost symmetric behavior about the $\mathrm{St}_j = 0$ line. In other words, each pair produces sum and difference frequency content of similar amplitude. The only noticeable deviation from symmetry is at the pair St_2 and St_a. The peak in the cross bicoherence at (St_2,St_a) is much more prominent than the peak at (St_2, $-\mathrm{St}_a$). Luckily, both narrow-band peaks at $\mathrm{St}_2 + \mathrm{St}_a$ and $\mathrm{St}_2 - \mathrm{St}_a$ overcome the broadband levels in the power spectrum, enabling us to confirm consistent trends (that is, the peak at $\mathrm{St}_2 + \mathrm{St}_a$ is larger in amplitude than $\mathrm{St}_2 - \mathrm{St}_a$ in the power spectrum). Again at higher angles of attack, i.e., $\alpha_h > 6^\circ$, no observable cross-bicoherence peaks are found.

These higher-order spectral results are valuable but do have limitations. To provide insight into what levels are significant, a random Gaussian signal is used to compute its autobicoherence and cross bicoherence with processing parameters (overlap, windowing, sampling frequency, and bin width) identical to those set for the actual data. In fact, such a signal is devoid of nonlinear interactions and thus helps quantify the noise floor of these computations. The mean autobicoherence value of this signal is approximately 0.0013 with an upper 2σ bound of 0.0015. The mean value of the Gaussian signal is plotted in Figs. 24 and 25.

Another limitation of these higher-order spectral methods is that they cannot reveal if mode switching occurs. However, there is a hump in the power spectrum (again, at low angles of attack) that corresponds uniquely to the arithmetic mean of St_2 and St_a, indicating such a behavior. While mode switching was not clearly observed in the spectrogram, other methods may extract visible evidence. For example, wavelet functions were used by Kegerise *et al.* [31], who visualized intermittent switching in a cavity flow. More specific to this problem, Li *et al.* [37] found switching between the primary spectral peaks on acoustic measurements of the 30P30N configuration. To this end, we suggest additional analysis of the unsteady surface pressure to get a better understanding of the possible intermittent behavior.

V. CONCLUSION

An extensive set of near-field measurements of the 30P30N slat cove has been analyzed. Particle image velocimetry data provide insight into the slat-cove flow field. The flow field was found to change with the angle of attack, namely, the path of the cove shear layer, the degree of unsteadiness at the cove shear layer reattachment point, and the trailing-edge wake properties. Mean spanwise vorticity profiles of the shear layer display a reasonable collapse with the angle of attack when the coordinate system is defined based on the shear layer path. Low angles generate a relatively large region of high $\mathcal{E}_{\text{turb}}$ at the shear layer impingement point. Vortical structures bombard the slat underside very close to the slat trailing edge, suggesting the large variance to be due to this interaction. Intermediate and high angles impinge on the slat surface farther from the trailing edge. Conversely, the shape of the trailing-edge wake profiles is not consistent with angle of attack. High angles display profiles similar to classic two-sided shedding, while low angles show single-side shedding on the upper side and additional mixing on the lower side (generating a broad vorticity hump). This additional mixing at low angles forces the trailing-edge wake to decay much more rapidly downstream.

Through the use of phase-locked PIV, the spectral peaks in the mid-Strouhal-number range [$O(1)$] found in the unsteady surface pressure spectra were generated by coherent shear layer structures, with the spatial wavelength of these structures related to each respective Strouhal number. An additional low-Strouhal-number hump was observed, which was linked to larger structures on the order of the size of the slat cove. A POD-based interpretation of this phenomenon suggests that this bulk cove oscillation is the cause of a shear layer flapping motion.

Unsteady surface pressure measurements also provided a great deal of information. Alongside evaluating trends in the pressure spectra with angle of attack, spanwise coherence length scales were also estimated. These scales at the narrow-band peak Strouhal numbers were found to exceed the slat chord at low angles, but found to drop to lower than $0.1s$ for angles greater than 5.5°.

Narrow-band peak Strouhal number prediction using the method in [14] were found to agree very well with the observed values by estimating the shear layer path length, convection velocity, and acoustic path length from the PIV data. Secondary peaks in the power spectrum are present at low angles which have been characterized as nonlinear interactions via higher-order spectral methods. The autobicoherence highlights the primary peaks displaying self-interaction, coupling with the bulk cove oscillation, and to a lesser extent coupling between flow-acoustic resonance mode pairs. However, nonlinearities only arise at low angles. Above $\alpha_h = 6^\circ$ the autobicoherence and cross bicoherence of all surface pressure signals barely exceed typical values of a Gaussian signal.

In conclusion, low angles of attack are associated with higher levels of unsteadiness as the cove shear layer impingement point is in close proximity to the slat trailing edge. Due to the fact that the mean vorticity distribution along the shear layer collapses with the angle of attack (Fig. 11), the shear layer itself is likely not responsible for this angle of attack dependence. Conversely, these results suggest that it is the interaction of the shear layer structures with the slat trailing edge. This is consistent with the lower-$\mathcal{E}_{\text{turb}}$ levels found at higher angles. Moreover, trailing-edge shedding is found to be very coherent at high angles as it becomes more independent of the cove shear layer, while the wake is effectively disorganized at low angles. In all, these results provide insight into the physical mechanisms responsible for the various noise sources and should prove invaluable in future modeling and noise-reduction efforts.

ACKNOWLEDGMENTS

The work reported here was performed under NASA Contract No. NNL13AE76P. The authors would like to thank Dr. M. Choudhari from NASA Langley Research Center for numerous insightful discussions.

[1] W. Dobrzynski, Almost 40 years of airframe noise research: What did we achieve? J. Aircraft **47**, 353 (2010).
[2] J. Mendoza, T. Brooks, and W. Humphreys, An aeroacoustic study of a leading edge slat configuration, Int. J. Aeroacoust. **1**, 241 (2002).
[3] M. Murayama, K. Nakakita, K. Yamamoto, H. Ura, Y. Ito, and M. M. Choudhari, in *Proceedings of the 20th AIAA/CEAS Aeroacoustics Conference, Atlanta, 2014* (AIAA, Reston, 2014), paper 2014–2080.
[4] C. Pagani, D. Souza, and M. Medeiros, Slat noise: Aeroacoustic beamforming in closed-section wind tunnel with numerical comparison, AIAA J. **54**, 1 (2016).
[5] K. A. Pascioni and L. N. Cattafesta, in *Proceedings of the 22nd AIAA/CEAS Aeroacoustics Conference, Lyon, 2016* (AIAA, Reston, 2016) p. 2960.
[6] F. R. d. Amaral, F. H. T. Himeno, C. d. C. Pagani, Jr., and M. A. F. de Medeiros, Slat noise from an MD30P30N airfoil at extreme angles of attack, AIAA J. **56**, 964 (2017).
[7] Y. Guo, K. Yamamoto, and R Stoker, Component-based empirical model for high-lift system noise prediction, J. Aircraft **40**, 914 (2003).
[8] B. L. Storms, J. A. Hayes, P. J. Moriarty, and J. C. Ross, in *Proceedings of the 5th AIAA/CEAS Aeroacoustics Conference and Exhibit* (AIAA, Reston, 1999), paper 1999–1957.
[9] C. C. Pagani, D. S. Souza, and M. A. F. Medeiros, Experimental investigation on the effect of slat geometrical configurations on aerodynamic noise, J. Sound Vib. **394**, 256 (2017).
[10] M. Pott-Pollenske, W. Dobrzynski, H. Buchholz, S. Guerin, G. Saueressig, and U. Finke, in *Proceedings of the 12th AIAA/CEAS Aeroacoustics Conference, Cambridge, 2006* (AIAA, Reston, 2006), paper 2006–2567.
[11] Y. Guo, Slat noise modeling and prediction, J. Sound Vib. **331**, 3567 (2012).
[12] M. Khorrami, M. Berkman, and M. Choudhari, Unsteady flow computations of a slat with a blunt trailing edge, AIAA J. **38**, 2050 (2000).
[13] B. A. Singer, D. P. Lockard, and K. S. Brentner, Computational aeroacoustic analysis of slat trailing-edge flow, AIAA J. **38**, 1558 (2000).
[14] M. Terracol, E. Manoha, and B. Lemoine, Investigation of the unsteady flow and noise generation in a slat cove, AIAA J. **54**, 469 (2016).
[15] J. Rossiter, Wind-tunnel experiments on the flow over rectangular cavities at subsonic and transonic speeds, Aeronautical Research Council Report No. 3438, 1966.
[16] M. Choudhari and D. Lockard, Assessment of Slat Noise Predictions for 30P30N High-Lift Configuration from BANC-III Workshop, in *Proceedings of the 21st AIAA/CEAS Aeroacoustics Conference, Dallas, 2015* (AIAA, Reston, 2015), pp. 1–41.
[17] M. Choudhari and M. Khorrami, Effect of three-dimensional shear-layer structures on slat cove unsteadiness, AIAA J. **45**, 2174 (2007).
[18] T. Knacke and F. Thiele, in *Proceedings of the 19th AIAA/CEAS Aeroacoustics Conference, Berlin, 2013* (AIAA, Reston, 2013), pp. 1–16.
[19] L. N. Jenkins, M. R. Khorrami, and M. Choudhari, in *Proceedings of the 10th AIAA/CEAS Aeroacoustics Conference* (AIAA, Reston, 2004), paper 2004–2801.
[20] K. Pascioni, R. Reger, A. Edstrand, and L. Cattafesta, Characterization of an Aeroacoustic Wind Tunnel Facility, in *Proceedings of the 43rd International Congress on Noise Control Engineering (Internoise 2014), Melbourne, 2014*.
[21] S. Klausmeyer and J. Lin, Comparative results from a CFD challenge over a 2D three-element high-lift airfoil, NASA Report No. TM 1997-112858, 1997.
[22] K. A. Pascioni, L. N. Cattafesta, and M. M. Choudhari, in *Proceedings of the 20th AIAA/CEAS Aeroacoustics Conference*, Atlanta, 2014 (Ref. [3]), paper 2014–3062.
[23] F. W. Spaid, High Reynolds number, multielement airfoil flowfield measurements, J. Aircraft **37**, 499 (2000).
[24] M. Choudhari, D. Lockard, M. Khorrami, and R. Minec, in *Proceedings of the 40th International Congress and Exposition on Noise Control Engineering (Internoise 2011), Osaka, 2011* (Curran, Red Hook, 2012).
[25] C. Rumsey, E. Lee-Rausch, and R. Watson, Three-dimensional effects in multi-element high lift computations, Comput. Fluids **32**, 631 (2003).

[26] K. Pascioni, An aeroacoustic characterization of a multi-element high-lift airfoil, Ph.D. thesis, Florida State University, 2017.
[27] J. Westerweel, Efficient detection of spurious vectors in particle image velocimetry data, Exp. Fluids **16**, 236 (1994).
[28] B. Wieneke, PIV uncertainty quantification from correlation statistics, Meas. Sci. Technol. **26**, 074002 (2015).
[29] A. K. M. F. Hussain and W. C. Reynolds, The mechanics of an organized wave in turbulent shear flow, J. Fluid Mech. **41**, 241 (1970).
[30] R. Thompson, A note on restricted maximum likelihood estimation with an alternative outlier model, J. R. Stat. Soc. B **47**, 53 (1985).
[31] M. Kegerise, E. Spina, S. Garg, and L. Cattafesta, Mode-switching and nonlinear effects in compressible flow over a cavity, Phys. Fluids **16**, 678 (2004).
[32] Y. Zhang, H. Chen, K. Wang, and M. Wang, Aeroacoustic prediction of a multi-element airfoil using wall-modeled large-eddy simulation, AIAA J. **55**, 4219 (2017).
[33] A. Mohammad-Taifour and J. Weiss, Unsteadiness in a large turbulent separation bubble, J. Fluid Mech. **799**, 383 (2016).
[34] L. Sirovich, Turbulence and the dynamics of coherent structures. Part 1: Coherent structures, Q. Appl. Math. **45**, 561 (1987).
[35] M. Terracol, E. Manoha, and E. Lemoine, in *Proceedings of the 20th AIAA Computational Fluid Dynamics Conference and Exhibit, Honolulu, 2011* (AIAA, Reston, 2011), paper 2011–3203.
[36] S. Hein, T. Hohage, W. Koch, and J. Schöberl, Acoustic resonances in a high-lift configuration, J. Fluid Mech. **582**, 179 (2007).
[37] L. Li, P. Liu, Y. Xing, and H. Guo, Time-frequency analysis of acoustic signals from a high-lift configuration with two wavelet functions, Appl. Acoust. **129**, 155 (2017).